ELSEVIER

Contents lists available at ScienceDirect

## Optics and Lasers in Engineering

journal homepage: www.elsevier.com/locate/optlaseng



# Compact snapshot dual-mode interferometric system for on-machine measurement



Daodang Wang<sup>a,b,\*</sup>, Xiangyu Fu<sup>a</sup>, Ping Xu<sup>a,c</sup>, Xiaobo Tian<sup>b</sup>, Oliver Spires<sup>b</sup>, Jian Liang<sup>b</sup>, Heng Wu<sup>b</sup>, Rongguang Liang<sup>b,\*\*</sup>

- <sup>a</sup> College of Metrology and Measurement Engineering, China Jiliang University, Hangzhou 310018, China
- <sup>b</sup> James C. Wyant College of Optical Sciences, University of Arizona, Tucson, Arizona 85721, USA
- <sup>c</sup> Guangxi Key Laboratory of Optoelectronic Information Processing, Guilin University of Electronic Technology, Guilin 541004, China

#### ARTICLE INFO

# Keywords: Optical interferometry Dual-mode interferometer Subaperture stitching On-machine measurement

#### ABSTRACT

To meet the need of on-machine metrology in optical manufacturing, a compact and snapshot dual-mode interferometric system is proposed for surface shape and roughness measurement. To simplify the measurement process between surface shape and roughness, a novel concept of using optical filters to separate the beam paths in the reference arm is introduced. A pixelated camera with a micro-polarizer array acquires four pi/2 phase-shifted interferograms simultaneously to minimize the environmental disturbance. Besides, the configuration-optimization-based subaperture stitching technique is introduced to extend the measurable aperture range. Both numerical analysis and experiments have been carried out to demonstrate the feasibility of the proposed compact snapshot dual-mode interferometer. The proposed system provides a powerful and portable tool to achieve on-machine surface characterization of various optical elements over a wide range of spatial frequencies and aperture sizes.

#### 1. Introduction

With increasing needs for high precision optical elements, accurate and efficient fabrication process is highly demanded, placing ultrahigh requirement on the measurement tools to improve workpiece quality control and manage machining process. As a recognized accurate testing method, the interferometry has been a powerful method for noncontact surface metrology of optical elements. Various laser interferometers, such as Fizeau interferometer, Twyman-Green interferometer, and point-diffraction interferometer [1-3], were developed for surface form metrology, which is the low spatial frequency form error. Surface roughness can be measured by the low coherence interference microscopes [4, 5] with either white light sources or light emitting diodes (LED). With the combination of laser interferometer and interference microscope, the surface characteristics of workpieces over a wide range of spatial frequencies can be accurately evaluated. Most of the commercially available interferometers, such as those from Zygo and 4D Technology, are designed in a single working mode, either interferometer mode or interference microscope mode. Thus, multiple measuring instruments are required to achieve the comprehensive evaluation of optical surface. Due to the limited space in the fabrication machine and accessibility of workpiece surface, the instrument for on-machine metrology should be compact enough. However, most of these commercial instruments are designed for off-line application and they are large in volume, not suitable for on-machine metrology. The workpiece has to be removed from the machine for off-line metrology and then re-positioned back to the machine for further process if the quality doesn't meet the specifications. This process is very time consuming, adding the cost and introducing additional fabrication errors.

Various on-machine and in-process measurement methods and systems have also been developed for ultra-precision machining systems, including interferometers [6–10], adaptive-optics-assisted system based on light scattering [11], chromatic confocal probe [12, 13], stereo vision method [14–16], and fringe deflectometry [17–21]. However, all these methods can only measure either surface shape or surface roughness. To meet the need for measuring both surface shape and roughness, a compact dual-mode snapshot interferometric system (DMSIS) (with the dimension of 304.8 mm  $\times$  304.8 mm  $\times$  76.2 mm) using Linnik configuration was proposed for on-machine metrology [22]. However, it adopts double source paths and requires the system reconfiguration (by removing the microscope objective in the reference arm) to switch the working mode, not compact or convenient enough for practical application.

E-mail addresses: wangdaodang@sina.com (D. Wang), rliang@optics.arizona.edu (R. Liang).

<sup>\*</sup> Corresponding author.

<sup>\*\*</sup> Corresponding author.

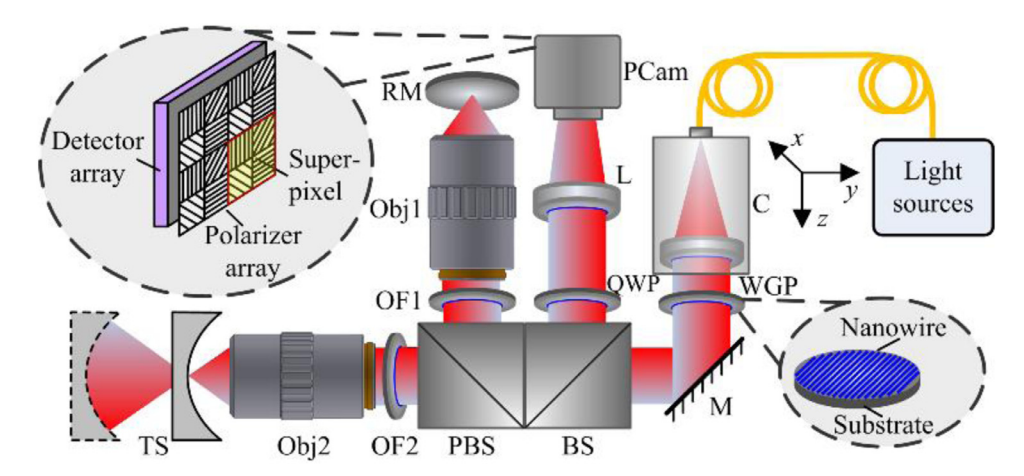


Fig. 1. System layout of compact snapshot dual-mode interferometer. C: optical collimator; WGP: wire grid polarizer; M: folding mirror; BS: beam splitter; PBS: polarized beam splitter; OF1: shortpass optical filter; OF2: longpass optical filter; Obj1 and Obj2: standard objective; TS: test sample; RM: reference mirror; QWP: quarter-wave plate; L: imaging lens; PCam: monochromatic polarization camera.

In this paper, a compact snapshot dual-mode interferometric system (SDIS) is proposed for the on-machine measurement of both optical surface shape and roughness. Using optical filters, dual working modes are achieved in an extremely compact configuration. To minimize the influence of environmental disturbances, a pixelated polarization camera is adopted to realize snapshot and fast measurement. Besides, the subaperture stitching technique based on configuration optimization is developed to extend the measurement range, enabling the testing of surfaces with large aperture. There are three main contributions of this work: (1) the proposed SDIS shares a single and almost "common-path" configuration setup for dual working modes, and it is extremely compact in configuration (with the dimension of 195 mm  $\times$  160 mm  $\times$  65 mm); (2) with the application of optical filters, no reconfiguration of internal system structure is needed to switch the working modes; (3) the extension in the measurable aperture range of the proposed compact interferometer is achieved based on the configuration-optimization-based subaperture stitching technique. All these features make it more practical and convenient for on-machine metrology. Sections 2 and 3 present the principle of the proposed SDIS, including the system configuration, system design, measurement range extension based on subaperture stitching technique, and error analysis. Section 4 shows the experimental results of on-machine tool alignment and large-aperture surface testing. Finally, some concluding remarks are drawn in Section 5.

#### 2. Principle

#### 2.1. System layout

The schematic diagram of the proposed SDIS is shown in Fig.1. Two light sources are used in the system: a laser (with the wavelength 632.8 nm) for surface shape measurement and a LED (with the central wavelength 540 nm and bandwidth 10 nm) for roughness measurement. Their spectrum are shown in Fig. 2. The light from the light source is coupled into an optical fiber (a single-mode optical fiber for laser and a multimode fiber for LED) and collimated by a collimator C, and then goes through a wire grid linear polarizer (WGP) with the transmission axis oriented at 45 ° to x-axis. By rotating the transmission axis of WGP, the relative intensity of test and reference arms can be adjusted to obtain the optimal fringe contrast. After reflected by the folding mirror M, the linearly polarized light passes through a beam splitter (BS). The pand s-polarized beams are transmitted and reflected from the polarizing beam splitter (PBS), respectively, serving as test and reference beams. To achieve the different working modes with a single system configuration, a high-performance shortpass optical filter OF1 (#84-710, Edmund Optics Inc., the rejection (reflection) wavelength range 614-900 nm and transmission wavelength range 350-587 nm) is placed in the reference arm to reflect the laser beam and transmit LED light for two different

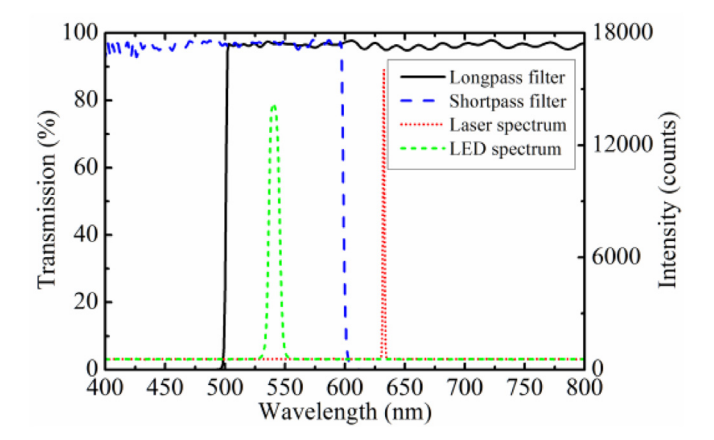


**Fig. 2.** Spectrum of the light sources and the transmission of the optical filters (#84-710 and #62-983, Edmund Optics) in the proposed SDIS.

measurement modes. To match the optical length difference (OPD), a longpass filter OF2 (#62-983, Edmund Optics Inc., the rejection wavelength range 200–490 nm and transmission wavelength range 508–1650 nm) with same thickness and material as the shortpass filter in the reference arm is added to the test arm between the objective Obj2 and PBS. The transmission of the longpass and shortpass filters at the wavelength range 400–800 nm are shown in Fig. 2.

To switch the working modes, the corresponding optical fibers with corresponding light sources can be connected to the source interface (that is the collimator C), making the system extremely convenient for practical on-machine metrology application. With the long working distance custom collimator, a dichroic mirror can be used to combine the laser light and LED light so that it is not necessary to switch the fibers, two different measurement modes can be switched by simply turning ON/OFF the laser or LED. In the interference microscope mode, the LED serves as light source, the test LED light passes the longpass filter OF2, and then is focused on test sample TS by the long working distance objective Obj2 (Mitutoyo Plan Apo 10 × and NA 0.28), the reference LED light goes through shortpass filter OF1 and is focused on the reference mirror RM by a matching objective Obj1 (Mitutoyo Plan Apo 10 × and NA 0.28). In the laser interferometer mode, the reference laser beam is reflected by the OF1, the test beam passes OF2 and is transformed to a spherical wave with Obj2 to match the test surface. By removing Obj2, the system is suitable for the flat surface testing.

The reflected test and reference beams are transmitted and reflected from the PBS, respectively, and then are reflected by the BS. A quarterwave plate (QWP) is used to transform the orthogonally linearly polarized test and reference beams to be oppositely circularly polarized. To meet the requirement of on-machine measurement, a pixelated polarization monochrome camera PCam from FLIR Systems Inc is used to capture the phase-shifted interferograms in a single shot. The Sony polarization image sensor (SONY IMX250MZR, resolution: 2448  $\times$  2048 pixels, pixel size: 3.45  $\mu$ m) inside PCam has a built-in micro-polarizer array with four linear polarizers at 0  $^{\circ}$ , 45  $^{\circ}$ , 90  $^{\circ}$  and 135  $^{\circ}$  adjacent to each other, forming a 2  $\times$  2 superpixel as shown in Fig. 1. It enables the snapshot capture of four interferograms with motionless phase shifting, therefore the system can make the real time on-machine measurement and is insensitive to environmental disturbance.

#### 2.2. Jones matrix description

In the proposed method, the polarization and propagation of the beams can be represented by Jones matrices. The Jones matrices for test beam  $(E_t)$  and reference beam  $(E_r)$  before the polarization camera are described as

$$\begin{cases} E_t = J_{QWP} \cdot T_{PBS} \cdot J_{TS} \cdot T_{PBS} \cdot E_{WGP} \\ E_r = J_{QWP} \cdot R_{PBS} \cdot J_{MR} \cdot R_{PBS} \cdot E_{WGP} \end{cases} \tag{1}$$

where  $E_{WGP}$ ,  $E_{QWP}$ ,  $J_{TS}$  and  $J_{MR}$  are the Jones matrices for the polarizer WGP, quarter-wave plate QWP, test sample TS and reference mirror RM;  $T_{PBS}$  and  $R_{PBS}$  are the transmittance and reflectance Jones matrices for the PBS. In the current configuration,  $T_{PBS} = [T_p, 0; 0, T_s]$  and  $R_{PBS} = [R_p, 0; 0, R_s]$ , where  $T_p$  and  $R_p$  are the transmittance and reflectance factors for p polarization,  $T_s$  and  $R_s$  are those for s polarization. Ideally,  $E_t$  and  $E_r$  can be simplified as  $E_t = A_t' \cdot \exp(i\varphi) \cdot [1, i]^T$  and  $E_r = A_r' \cdot [1, -i]^T$ , where  $\varphi$  is the phase difference related to test sample surface,  $A_t'$  and  $A_r'$  are the corresponding Jones matrix coefficients. Thus, the Jones matrices for the interfering test wave  $(E_{t,j}')$  and reference wave  $(E_{r,j}')$  after going through the micro-polarizer array in PCam are

$$\begin{cases} E'_{t,j} = A_j \cdot E_t = \begin{bmatrix} \cos^2 \theta & \cos \theta \sin \theta \\ \cos \theta \sin \theta & \sin^2 \theta \end{bmatrix} \cdot E_t \\ E'_{r,j} = A_j \cdot E_r = \begin{bmatrix} \cos^2 \theta & \cos \theta \sin \theta \\ \cos \theta \sin \theta & \sin^2 \theta \end{bmatrix} \cdot E_r \end{cases}$$
(2)

where  $A_j$  (j=1, 2, 3, 4) is the Jones matrix for the micro-polarizer with transmission axis oriented at the angle  $\theta$  ( $\theta$ =0°, 45°, 90°, 135°) to x-axis. The superposition of test and reference waves in different micro-polarizer orientations is defined as  $E'_j = E'_{t,j} + E'_{r,j}$ , and the corresponding intensity recorded on the camera is  $I_j = |E'_j(1)|^2 + |E'_j(2)|^2$ . Thus, the phase difference  $\varphi$ , which corresponds to the optical path difference between the test and reference surfaces, can be calculated with four-step phase shifting algorithm,

$$\varphi = \tan^{-1} \left( \frac{I_2 - I_4}{I_1 - I_3} \right). \tag{3}$$

#### 2.3. Extension of measurement range based on subaperture stitching

The compact configuration of the proposed SDIS enables on-machine measurement; however, its measurement range for convex surface is limited due to the small aperture of the microscope objective. To extend the measurement range, the subaperture stitching technique is developed. Besides, the subaperture configuration optimization is used to loose the requirement on the precision of subaperture positioning system, enabling the general application of the proposed system with a simple and less precision motion mechanism.

#### 2.3.1. Subaperture stitching algorithm

In practical subaperture stitching measurement, the relative misalignment could exist in the overlapping areas among adjacent subapertures, and it can be eliminated by removing the piston, tilt and defocus coefficients of each subaperture [23]. The  $N_{th}$  subaperture in the multiple subaperture measurements could be chosen as the reference subaperture, and the relative phase  $\varphi_i'$  of the phase  $\varphi_i$  in the  $i_{th}$  subaperture

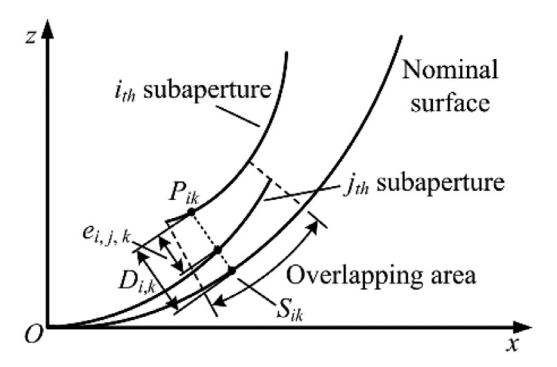


Fig. 3. Schematic diagram of projection in overlapping calculation.

with respect to the reference subaperture can be represented as

$$\varphi'_{i,i\neq N} = \varphi_i + T_{x,i} + T_{y,i} + B_i(x^2 + y^2) + C_i, \tag{4}$$

where  $T_{x,i}$ ,  $T_{y,i}$ ,  $B_i$  and  $C_i$  are the coefficients of the tilts in x and y directions, defocus and piston of each subaperture. The coefficients ( $T_{x,i}$ ,  $T_{y,i}$ ,  $B_i$ ,  $C_i$ ) of each subaperture need to be optimized to fit the full aperture, and they could be obtained with the least square fitting method by minimizing the sum of squared differences of phase in the overlapped areas.

$$\min = \sum_{i} \sum_{j}^{j \cap i} \left\{ \left[ \varphi_{i} + T_{x,i} + T_{y,i} + B_{i}(x^{2} + y^{2}) + C_{i} \right] - \left[ \varphi_{j} + T_{x,j} + T_{y,j} + B_{j}(x^{2} + y^{2}) + C_{j} \right] \right\}^{2}.$$

$$(5)$$

#### 2.3.2. Subaperture configuration optimization

The accuracy and reliability of subaperture stitching depend on the precision of the subaperture positioning system. A five-axis (or six-axis) precision motion mechanism is traditionally used for subaperture positioning. To improve the robustness of subaperture stitching interferometric testing with the proposed SDIS, the subaperture configuration optimization is carried out to minimize the mismatch in the overlapped areas among subapertures [24]. Based on the three-dimensional coordinate transformation, the local coordinates  $(x_{ik}, y_{ik}, z_{ik})$  of the  $k_{th}$  sampling point in the  $i_{th}$  subaperture can be converted to the corresponding global coordinates  $P_{ik}$ 

$$P_{ik} = g_i^{-1} [x_{ik}, y_{ik}, z_{ik}, 1]^T,$$
(6)

where  $g_i$  is the transformation matrix representing the configuration of full-aperture frame with regard to the  $i_{th}$  subaperture. In the case of subaperture positioning with less precision motion mechanism, the transformation matrices  $\{g_i\}$  needs to be optimized to minimize the mismatch in the overlapped area. All the points  $\{P_{ik}\}$  in the  $i_{th}$  subaperture are projected onto the nominal full-aperture surface (as shown in Fig. 3) and the corresponding projection points are  $\{S_{ik}\}$ . For the corresponding points in the overlapped area in the  $i_{th}$  and  $j_{th}$  subapertures, the deviation  $e_{i,j,k}$  between their distance  $D_{i,k}$ ,  $D_{j,k}$  to nominal surface is given as

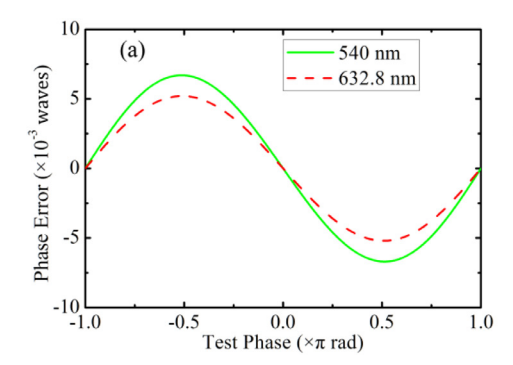
$$e_{i,j,k} = D_{i,k} - D_{j,k}. (7)$$

Thus, bi-objective linear combination can be used as the objective function in the subaperture configuration optimization,

$$\min Obj = \varepsilon_1 \sigma^2 + \varepsilon_2 \sigma_0^2, \tag{8}$$

where  $\varepsilon_1$  and  $\varepsilon_2$  are the positive weights, and  $\varepsilon_1 + \varepsilon_2 = 1$ ;  $\sigma$  and  $\sigma_0$  are the root mean square (RMS) values of the directed distances  $\{D_{i,k}\}$  to nominal surface and the distance deviations  $\{e_{i,k,k}\}$ , respectively,

$$\begin{cases} \sigma^2 = \sum_{i} \sum_{k} D_{i,k}^2 / \sum_{i} N_i \\ \sigma_0^2 = \sum_{i} \sum_{j} \sum_{k} e_{i,j,k}^2 / N_{total} \end{cases}$$
(9)



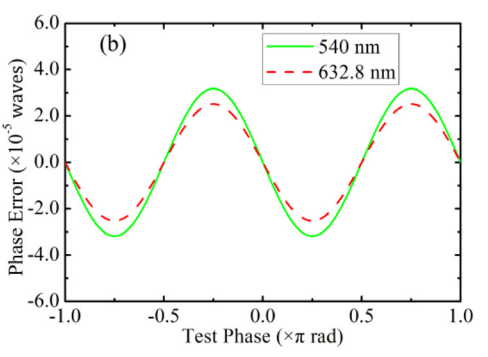


Fig. 4. Phase error due to imperfection of polarization optics in the SDIS: (a) PBS, (b) QWP.

where  $N_i$  is the total number of sampling points within the  $i_{th}$  subaperture, and  $N_{total}$  is the total number of overlapping points of all subapertures. According to Eq. (8), the subaperture configuration parameters  $\{g_i\}$  can be optimized by minimizing the objective function Obj.

#### 3. Error considerations

The application of pixelated polarization camera for simultaneous phase-shifting interferometric testing makes the proposed SDIS insensitive to environmental disturbance; however, the imperfect performance of the components, mainly the polarization optical components and polarization camera, used in the system could introduce the measurement errors.

#### 3.1. Imperfection of optical components

Polarization optical elements are key in the proposed SDIS as the test and reference beams are polarized. A wire grid polarizer with contrast ratios of 3737 and 2745 at 632.8 and 540 nm is utilized in the system to obtain an input beam with high-degree linear polarization. To meet the requirement of two measurement modes at two wavelengths, the broadband PBS and achromatic QWP are adopted in the system.

The PBS is used to separate the p-polarized test wave and s-polarized reference wave. For the broadband PBS in the system, the transmissions for p- and s-polarized light at the wavelength 632.8 nm are 96.0% and 0.04%, respectively, and those at the wavelength 540 nm are 96.9% and 0.07%. According to Eq. (1), the corresponding phase error due to the imperfection of PBS is shown in Fig. 4(a), with the peak to valley (PV) value of 0.0134 waves at 540 nm and 0.0104 waves at 632.8 nm. Besides, the retardances of QWP at the working wavelengths 540 nm and 632.8 nm are 0.2455 waves and 0.2460 waves, respectively. Fig. 4(b) shows the phase error introduced by QWP at 540 nm and 632.8 nm, PV values are  $6.4 \times 10^{-5}$  waves and  $5.0 \times 10^{-5}$  waves, respectively, and they are negligible.

To achieve two measurement modes in a single compact configuration, the shortpass filter OF1 is used to reflect the laser beam and transmit the LED light, and the longpass filter OF2 is adopted to match the optical path. Using the dichroic filters, the rejection wavelengths are reflected, while transmission wavelengths are transmitted. In the laser interferometer mode, the form error on the incident surface on OF1 and transmitting aberration of OF2 could introduce measurement error; for the interference microscope mode, the transmitting aberrations of both filters could introduce measurement error. However, the systematic error from both the filters can be pre-measured and removed after the calibration.

#### 3.2. Imperfection of polarization camera

Due to the imperfect performance of the micro-polarizer array in polarization camera PCam, several error factors, including the crosstalk among polarization channels, photon response nonuniformity (PRNU),

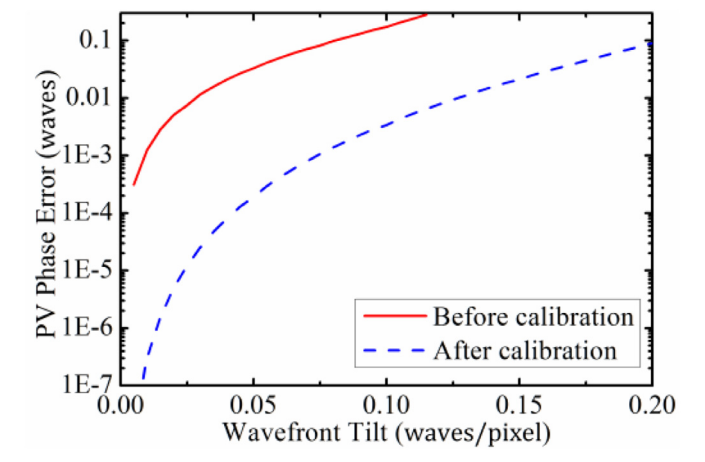


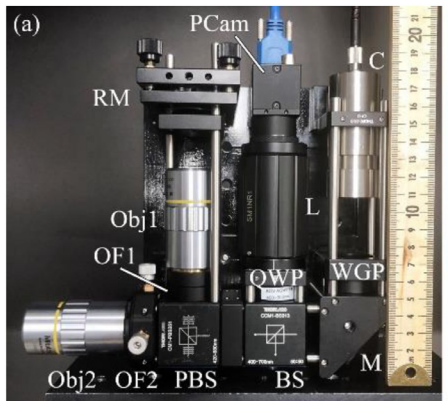
Fig. 5. Calibration of FOV error in monochromatic polarization camera.

micro-polarizer extinction ratio nonuniformity (ERNU) and micro-polarizer orientation misalignment (POMA), may introduce an additional measurement error. Various calibration methods have been developed to reduce the errors related to the micro-polarizer array. Compared to the polarization camera with polarizer array installed above the on-chip lens layer, Sony polarization CMOS sensor IMX250MZR has the polarizer array formed under on-chip lens layer, improving the performance of polarization camera to a tremendous extent. The channel crosstalk, PRNU, ERNU and POMA are significantly reduced.

To calculate the phase using Eq. (3), the assumption is that the phase over a  $2 \times 2$  superpixel region remains constant, however, this is not the case in actual application. This is the field of view (FOV) error and should be minimized [25]. To minimize the FOV error, the linear-spline interpolation of neighboring pixels with the same polarization orientation over a  $3 \times 3$  pixel grid can be applied to retrieve the missing intensity values of all the pixels. Fig. 5 shows the corresponding phase calculation error under various wavefront tilts before and after calibration. According to Fig. 5, FOV error increases significantly with larger wavefront tilt, and the calibration method based on linear-spline interpolation provides a feasible way to minimize FOV error. High calibration accuracy for FOV error can be achieved even for the high local wavefront tilt of 0.12 waves/pixel, with the PV value of residual phase error decreasing from over 0.2800 to 0.0078 waves.

#### 4. Experimental results and analysis

The prototype of the proposed SDIS has been built with commercial components to evaluate its performance and feasibility, Fig. 6(a) shows the system layout, it is very compact with the dimension of 195 mm  $\times$  160 mm  $\times$  65 mm, extremely suitable for on-machine measurement. The dimension can be further reduced by custom components. The experimental demonstration (as shown in Fig. 6(b)) was carried out in



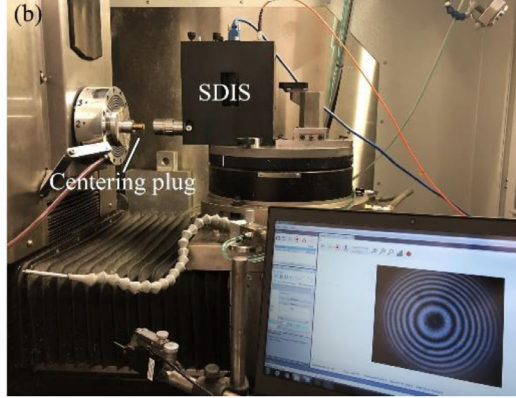


**Fig. 6.** On-machine measurement with SDIS on the diamond turning machine. (a) system layout, (b) on-machine measurement.

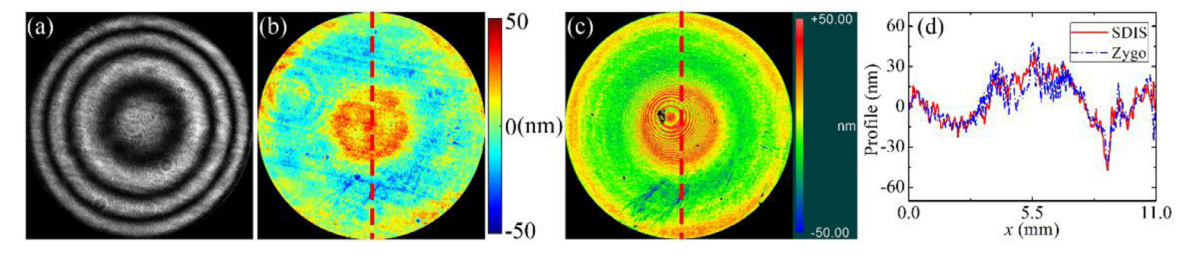


Fig. 7. Surface shape of the centering plug for tool alignment in diamond turning machine. (a) Interferogram and (b) surface shape acquired with on-machine SDIS, (c) surface shape from off-machine Zygo interferometer, and (d) line profile comparison.

Moore Nanotech 350 FG diamond turning machine for tool alignment. Besides, a reflective surface with large aperture was also measured with SDIS to validate the feasibility of the SDIS in large-aperture surface measurement.

### 4.1. On-machine tool alignment

Generally, a centering plug is used for the tool alignment in diamond turning machine. The proposed SDIS provides a powerful tool for the onmachine measurement of the centering plug. The SDIS was mounted on the B-axis rotation stage. Before tool alignment, a test flat mirror was placed on the spindle, and the misalignment between the spindle C-axis and optical axis of SDIS was calibrated by nulling the interferogram. A convex surface with a radius of 19.985 mm was cut on the 11mm diameter centering plug, the surface shape and roughness were then measured with the SDIS on the machine. In addition, the off-machine control experiments with Zygo Verifire laser interferometer and Zygo NewView 8300 optical surface profiler were also carried out for comparison.

For the small-aperture centering plug, the full-aperture surface measurement can be achieved by the SDIS. Fig. 7 shows the measured surface map of the centering plug with SDIS and Zygo interferometer, respectively. The PV and RMS values of surface map (Fig. 7(b)) in the on-machine measurement with SDIS are 0.1276  $\mu m$  and 0.0147  $\mu m$ , respectively, and those (Fig. 7(c)) with off-machine Zygo interferometer are 0.1142  $\mu m$  and 0.0123  $\mu m$ . The line profile comparison of the measured surface with these two systems is given in Fig. 7(d). It can be seen from Fig. 7 that a good agreement between SDIS and off-machine measurement is obtained. The map error and noise in SDIS is slightly larger than that in Zygo interferometer, which is mainly due to residual systematic error from the imperfect optical elements. In addition, small rings can be seen in the central region of the measured map with Zygo interferometer, it is caused by the attenuation film.

Fig. 8 shows the measured surface roughness of the centering plug with SDIS and Zygo profilometer, the measurement area is about 600  $\mu$ m × 600  $\mu$ m. The PV, RMS and Ra (arithmetical mean roughness) values measured with SDIS (Fig. 8(b)) are 0.5391  $\mu$ m, 0.0082  $\mu$ m and 0.0041  $\mu$ m, respectively, and those (Fig. 8(c)) with Zygo profilometer

are 0.5286  $\mu$ m, 0.0071  $\mu$ m and 0.0041  $\mu$ m. The line profile comparison of the measured surface roughness with these two systems is given in Fig. 8(d). Thus, a measurement consistency with SDIS and Zygo profilometer is achieved, both in the surface roughness and magnitude. Several factors could lead to the minor difference between on- and offmachine measurement results, such as the cutting debris (bottom left region in Figs. 8(a) and (b)), residual systematic error and different bandwidth of LED light sources. Due to the fact that the FOV of SDIS ( $\sim 600~\mu$ m  $\times 600~\mu$ m) is smaller than that of Zygo profilometer ( $\sim 834~\mu$ m  $\times 834~\mu$ m), as well as the fact that the sensor in SDIS has more pixels than that in Zygo profilometer (5M vs. 1M pixels), higher spatial resolution is obtained with SDIS within the same measurement area, thus, more obvious tool marks can be seen in Fig. 8(b).

#### 4.2. Large-aperture surface measurement

To validate the feasibility of the proposed SDIS to measure largeaperture surfaces, a concave spherical surface with 50 mm diameter and 34 mm curvature radius was cut and tested. The test surface was installed on a five-axis low-precision motion stage (angular positioning accuracy about y- and z-axes: 2°; linear positioning accuracy in x-, y-, and z-axes: 10  $\mu$ m), and 16 subapertures were individually measured with SDIS and then stitched to cover the full aperture of test surface. To improve the subaperture stitching accuracy with the proposed SDIS, the subaperture configuration optimization (SCO) has been performed. Fig. 9 shows the objective function with the iteration number in the optimization process, and it rapidly converges after 4 iteration cycles. Fig. 10 shows the comparison of the measured surface shapes in the experiment. Figs 10(a) and (d) are the stitched surface map and subaperture distribution based on the original subaperture configuration parameters, obvious mismatch among subapertures can be observed. The stitched surface and subaperture distribution after 6 optimization cycles are shown in Figs. 10(b) and (e), respectively. It can be seen from Figs. 10(b) and (e) that the configuration parameters are well optimized. Besides, a control experiment with Zygo interferometer has also been carried out, and Fig. 10(c) shows the corresponding measured full-aperture surface map. The measurement results are summarized in Table 1.

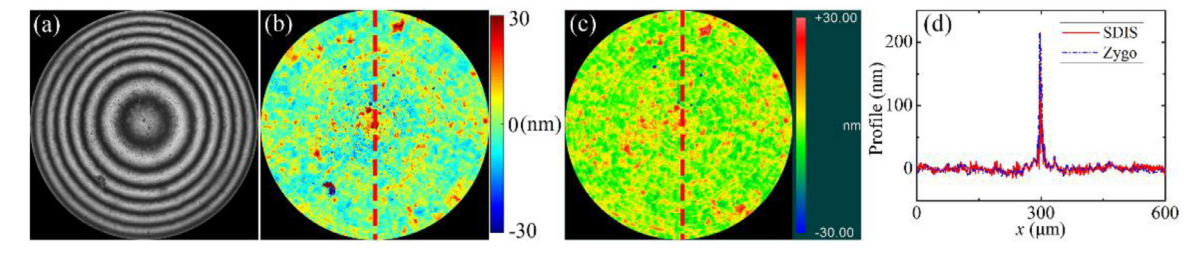


Fig. 8. Surface roughness of the centering plug. (a) Interferogram and (b) surface roughness acquired with on-machine SDIS, (c) surface roughness from off-machine Zygo profilometer, (d) line profile comparison.

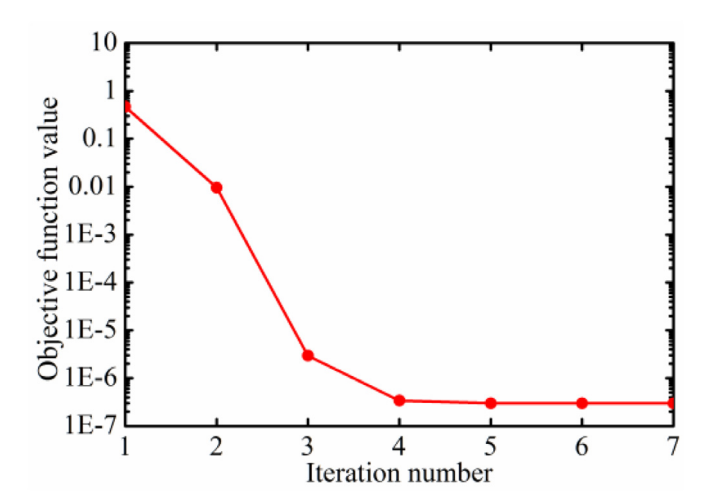


Fig. 9. Iteration curve in the optimization process of subaperture stitching.

Compared with the Zygo interferometer testing result in Fig. 10(c), the absolute PV and RMS differences in Fig. 10(b) are 0.2897  $\mu$ m and 0.0107  $\mu$ m, respectively, thus a good agreement is obtained. According to Fig. 10 and Table 1, the proposed SDIS with combination of

**Table. 1**Comparison of large-aperture spherical surface testing results in the experiment.

	Surface map		Testing error	
	PV $(\mu m)$	RMS $(\mu m)$	PV (μm)	RMS ( $\mu$ m)
Zygo interferometer	8.2995	1.5131		
SDIS before SCO	8.9142	1.4944	0.6147	-0.0187
SDIS after SCO	8.5892	1.5238	0.2897	0.0107

configuration-optimization-based subaperture stitching technique enables the large-aperture surface measurement, and high testing accuracy can be achieved even with less precision motion mechanism. Several factors could lead to the measurement error in the large-aperture surface testing with SDIS, including those from individual subaperture interferometric measurement and subaperture stitching process. According to the analysis in Section 3, the systematic errors due to the imperfection of system components can be well eliminated in each individual subaperture measurement; besides, the individual testing results can be averaged from multiple measurements to minimize the effect of random errors (such as electrical noise and environmental disturbance). The stitching error mainly results from the subaperture positioning errors due to motion mechanism and convergent accuracy of the stitching algorithm. The stitching algorithm based on subaperture configuration optimization is high in convergent accuracy (Fig. 9), thus, the measure-

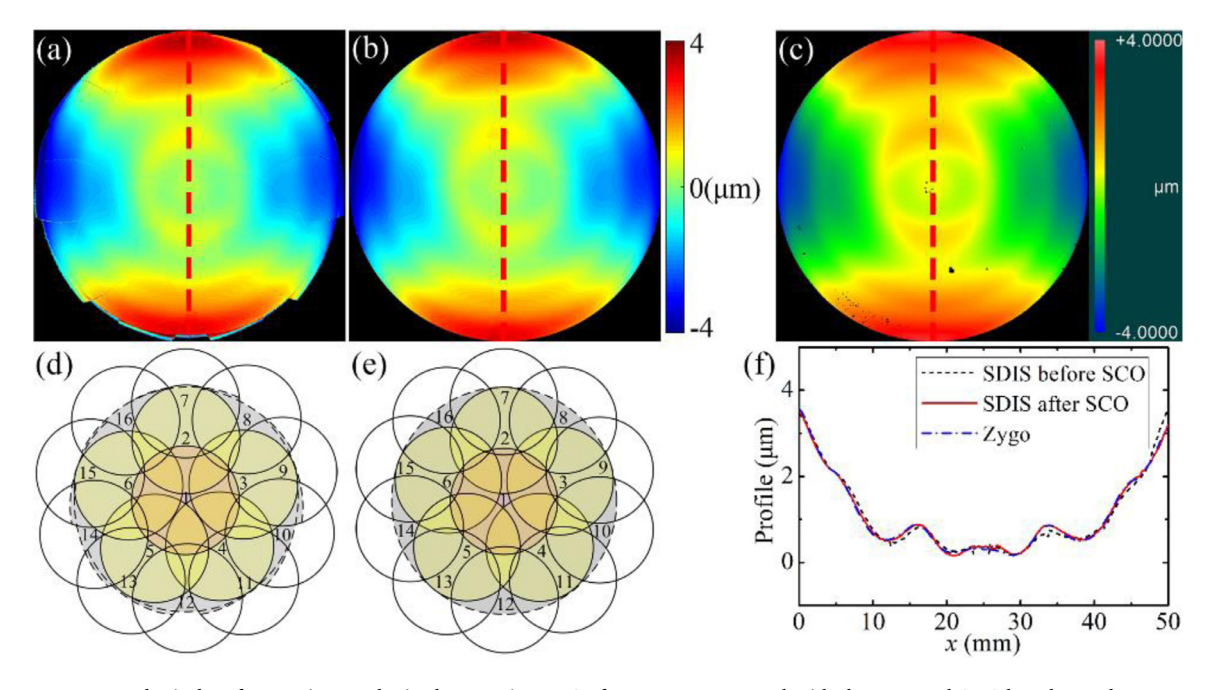


Fig. 10. Large-aperture spherical surface testing results in the experiment. Surfaces errors measured with the proposed SDIS based on subaperture stitching (a) before and (b) after subaperture configuration optimization (SCO), and (c) Zygo interferometer; subapertures (d) before and (e) after subaperture configuration optimization; (f) line profile comparison.

ment error from the stitching algorithm is negligible. It also can be seen from the subaperture distributions in Figs. 10(d) and (e), the subaperture configuration optimization performed in the stitching process enables the effective compensation of the subaperture positioning errors. Due to the fact that the residual measurement error could still exist in an individual subaperture, it can be accumulated in the stitching process. By reducing the subaperture number, the measurement accuracy is expected to be further improved.

#### 5. Conclusion

A compact, snapshot dual-mode interferometric system has been proposed for on-machine measurement. The proposed system enables the measurement of both surface shape and roughness, and can also achieve large-aperture surface testing with configuration-optimization-based subaperture stitching technique. Both the feasibility and measurement accuracy are experimental validated. The proposed SDIS is insensitive to environmental disturbance and is compact in system configuration. Thus, it is a powerful and portable tool for the real-time and on-machine surface characterization of various optical elements over a wide range of spatial frequencies and aperture sizes.

#### 6. Funding

This work is supported by National Natural Science Foundation of China (NSFC) (51775528), Guangxi Key Laboratory of Optoelectronic Information Processing (GD18205), China Postdoctoral Science Foundation (2017M621928), National Science Foundation (NSF) (1455630 and 1918260), National Institutes of Health (NIH) (S100D018061).

#### **Declaration of Competing Interest**

None.

#### CRediT authorship contribution statement

Daodang Wang: Conceptualization, Methodology, Investigation, Writing - original draft. Xiangyu Fu: Software, Validation. Ping Xu: Software, Writing - review & editing. Xiaobo Tian: Visualization, Investigation. Oliver Spires: Validation. Jian Liang: Writing - review & editing. Heng Wu: Writing - review & editing. Rongguang Liang: Conceptualization, Writing - original draft, Supervision, Funding acquisition.

#### References

 Wang D, Yang Y, Chen C, Zhuo Y. Point diffraction interferometer with adjustable fringe contrast for testing spherical surfaces. Appl Opt 2011;50:2342–8.

- [2] Yamamoto K, Matsuo T, Imada H, Kino M. Measurement of complex amplitude with a point-diffraction interferometer. Appl Opt 2015;54:7895–903.
- [3] Wang D, Xu Y, Liang R, Kong M, Zhao J, Zhang B, Li W. High-precision method for submicron-aperture fiber point-diffraction wavefront measurement. Opt Express 2016:24:7079–90
- [4] Wyant J, Schmit J. Computerized interferometric measurement of surface microstructure. Proc SPIE 1996;2782:26–37.
- [5] Wang D, Liang R. Simultaneous polarization Mirau interferometer based on pixelated polarization camera. Opt Lett 2016;41:41–4.
- [6] Millerd J, Brock N, Hayes J, North-Morris M, Novak M, Wyant J. Pixelated phase-mask dynamic interferometer. Proc SPIE 2004;5531:304–14.
- [7] Jiang X, Wang K, Martin H. Near common-path optical fiber interferometer for potentially fast on-line microscale-nanoscale surface measurement. Opt Lett 2006;31:3603-5.
- [8] Yan JW, Baba H, Kunieda Y, Yoshihara N, Kuriyagawa T. Nano precision on-machine profiling of curved diamond cutting tools using a white-light interferometer. Int J Surf Sci Eng 2007;1:441–55.
- [9] Jiang X. In situ real-time measurement for micro-structured surfaces. CIRP Ann— Manuf Techn 2011;60:563–6.
- [10] Yang SM, Zhang GF. A review of interferometry for geometric measurement. Meas Sci Technol 2018;29:102001.
- [11] Fuh YK, Hsu KC, Fan JR. Rapid in-process measurement of surface roughness using adaptive optics. Opt Lett 2012;37:848–50.
- [12] Zou XC, Zhao XS, Li G, Li ZQ, Sun T. Non-contact on-machine measurement using a chromatic confocal probe for an ultra-precision turning machine. Int J Adv Manuf Technol 2017;90:2163–72.
- [13] Chen XG, Nakamura T, Shimizu Y, Chen C, Chen YL, Matsukuma H, Gao W. A chromatic confocal probe with a mode-locked femtosecond laser source. Opt Laser Technol 2018;103:359–66.
- [14] Tian X, Deng H, Fujishima M, Yamazaki K. Quick 3D Modeling of machining environment by means of on-machine stereo vision with digital decomposition. Cirp Ann-Manuf Techn 2007;56:411–14.
- [15] Chen LC, Nguyen XL. Dynamic 3D surface profilometry using a novel colour pattern encoded with a multiple triangular model. Meas Sci Technol 2010;21:054009.
- [16] Sims-Waterhouse D, Piano S, Leach R. Verification of micro-scale photogrammetry for smooth three-dimensional object measurement. Meas Sci Technol 2017;28:055010.
- [17] Faber C, Olesch E, Krobot R, Hausler G. Deflectometry challenges interferometry the competition gets tougher!. Proc SPIE 2012;8493:84930R.
- [18] Oh CJ, Lowman AE, Smith GA, Su P, Huang R, Su T, Kim D, Zhao C, Zhou P, Burge JH. Fabrication and testing of 4.2m off-axis aspheric primary mirror of Daniel K. Inouye Solar Telescope Proc SPIE 2016;9912:99120O.
- [19] Choi H, Trumper I, Dubin M, Zhao W, Kim DW. Simultaneous multi-segmented mirror orientation test system using a digital aperture based on sheared Fourier analysis. Opt Express 2017;25:18152–64.
- [20] Wang D, Xu P, Gong Z, Xie Z, Liang R, Xu X, Kong M, Zhao J. Transmitted wavefront testing with large dynamic range based on computer-aided deflectometry. J Optics 2018:20:065705.
- [21] Wang D, Gong Z, Xu P, Wang C, Liang R, Kong M, Zhao J. Accurate calibration of geometrical error in reflective surface testing based on reverse Hartmann test. Opt Express 2018;26:8113–24.
- [22] Tian X, Zhang Y, Sohn A, Spires OJ, Liang R. Dual-mode snapshot interferometric system for on-machine metrology. Opt Eng 2019;58:044104.
- [23] Zhao C, Burge JH. Stitching of off-axis sub-aperture null measurements of an aspheric surface. Proc SPIE 2008;7063:706316.
- [24] Chen S, Li S, Dai Y. Iterative algorithm for subaperture stitching interferometry for general surfaces. J Opt Soc Am A 2005;22:1929–36.
- [25] Novak M, Millerd J, Brock N, North-Morris M, Hayes J, Wyant J. Analysis of a micropolarizer array-based simultaneous phase-shifting interferometer. Appl Opt 2005;44:6861–8.